Solar Energy Advances 6 (2026) 100146

Contents lists available at ScienceDirect

Solar Energy Advances

journal homepage: www.elsevier.com/locate/seja

Conceptual design and initial assessment of a solar CPC-concrete thermal energy storage system for industrial process heat in Uruguay

Pedro Galione[a,*], Germán Navarrete[a], Renzo Guido Cruz[a], Federico Licandro[a], Juan Rodríguez Muñoz[b], Italo Bove[a], Joaquin Buydid[c], Sebastián Lillo[a], Pablo Dellicompagni[d], Marcos Hongn[d], Loreto Valenzuela[e], Emmanuel Romano[c]

[a] Facultad de Ingeniería, Universidad de La República, Montevideo, Uruguay
[b] Laboratorio de Energía Solar, Universidad de la República, Salto, Uruguay
[c] Völfer Ingeniería, Paso de los, Toros, Uruguay
[d] Instituto de Investigaciones en Energía no Convencional, Salta, Argentina
[e] CIEMAT-Plataforma Solar de Almería, Almería, Spain

ARTICLE INFO

Keywords:
Solar heat for industrial process
CPC collectors
Concrete thermal energy storage
Academia–industry collaboration
Pilot prototype

ABSTRACT

This work presents the design and preliminary assessment of a Solar Heat for Industrial Processes (SHIP) pilot system developed in Uruguay for operation in the 100–150°C range. The proposed system integrates a non-tracking compound parabolic collector (CPC) field with a concrete-based thermal energy storage (TES) unit within a closed-loop pressurized water–glycol circuit, designed to emulate industrial steam demand through a tank–coil heat exchanger. It is designed for a nominal thermal output of 10 kW and an aperture area of ~25 m^2, prioritizing local manufacturability and operational simplicity. The design methodology combines simplified analytical models, numerical simulations (optical and thermal), and experimental testing to support component sizing and performance prediction. Experimental characterization of the collector follows ISO 9806:2025 procedures at the Laboratorio de Energía Solar, while TES design is supported by numerical modeling and laboratory evaluation of concrete formulations. Preliminary results from a 3.9 m^2 CPC prototype show a peak optical efficiency of 33.5%, below the expected range, with analysis indicating that thermal losses remain within design values and that performance deviations are mainly associated with optical and manufacturing factors. For the TES, thermal conductivities of up to 2.65 W/m·K were measured for selected concrete mixes, although variability in the measurements highlights the need for further testing. Numerical results indicate that the proposed configuration supports thermal stratification and effective charge–discharge behavior. Overall, the proposed methodology supports the conceptual design and preliminary assessment of the SHIP pilot plant and provides a sound basis for further experimental validation and techno-economic assessment.

List of Acronyms

ACPA	aged commercial polished aluminum
ASTM	American Society for Testing and Materials
BECS	Solar Water Heater Test Bench (at Universidad de la República in Salto (Uruguay))
CBA	choosing by advantages
CNC	computer numerical control
CPA	commercial polished aluminum
CPC	compound parabolic collector
CPSS	commercial polished stainless steel
CR	concentration ratio
DP	parabolic dish concentrator
ETC	evacuated tube collector
HP	heat pipe
HR	heat charging rate
HRAB	high-reflectance aluminum
IAM	incidence angle modifier
ISO	International Organization of Standarization
LFR	linear Fresnel reflector
NTU	number of transfer units
PLC	programmable logic controller

* Corresponding author.
E-mail address: pgalione@fing.edu.uy (P. Galione).

https://doi.org/10.1016/j.seja.2026.100146
Received 18 September 2025; Received in revised form 1 July 2026; Accepted 31 July 2026
Available online 13 August 2026

PTC	parabolic trough collector
SHIP	solar heat for industrial processes
SOC	state of charge
SWC	Solar World Congress
TC	central tower systems
TES	thermal energy storage
VFD	variable-frequency drive

Introduction

The industrial sector remains one of the primary contributors to global greenhouse gas emissions, largely due to its heavy reliance on fossil fuels for thermal processes. Specifically, industries such as food processing, chemical production, and general manufacturing require process heat, often in the form of steam, in the medium-temperature range of 100–200°C [1,2]. While renewable electricity has seen significant growth, technologies for renewable industrial heat remain underutilized. In this context, solar heat for industrial processes (SHIP) is gaining traction as a key strategy for industrial decarbonization [3–6].

This project, launched in 2024 as a collaboration between academic researchers and a local metal-mechanical company, focuses on the development of a solar thermal system designed to provide both solar heat generation and thermal energy storage. The objective is to achieve a cost-effective solution, competitive with fossil fuel alternatives, using a preliminary viability threshold of 500 USD/m^2 [1] [1]. This paper presents the design, fabrication, and assembly of the prototype, together with preliminary experimental and numerical results, while full-system operation and techno-economic evaluation are left for future work.

Solar heat for industrial processes

SHIP has received increasing attention as a pathway for decarbonizing industrial energy demand. Recent studies and international reports highlight the growing deployment of SHIP technologies worldwide, although their contribution to the global energy mix remains limited [3,5]. These reports provide comprehensive assessments of installed capacity, technology trends, and the role of solar thermal systems in reducing fossil fuel consumption and CO_2 emissions.

To address heat production above 100°C, several technological alternatives exist, including parabolic trough collectors (PTC), compound parabolic collectors (CPC), linear Fresnel reflectors (LFR), central tower systems (TC), and parabolic dish concentrators (DP) [7,8]. While these technologies are commercially available worldwide, the Uruguayan solar thermal market is currently limited to low-temperature applications such as domestic hot water, primarily using flat-plate and evacuated tube collectors. Although there is some local research experience in PTC development [9,10] and in feasibility analyses of PTC and Fresnel technologies [1,11], there are no commercial installations in the country supplying heat above 100°C.

Technologies capable of operating efficiently in this temperature range generally require solar concentration. PTC and LFR systems utilize solar tracking to reach temperatures up to 400°C, but involve higher structural and operational complexity. In contrast, CPC collectors provide moderate concentration on a linear absorber without requiring solar tracking, making them particularly suitable for the 100–150°C range [8]; [12,2], with potential for higher temperatures under optimized conditions [5].

For this project, the technology selection was guided by the Choosing by Advantages (CBA) methodology [13]. The objective was to identify a system capable of reliably delivering steam in the 100–150°C range while maximizing local manufacturing and minimizing operational complexity and risk. The evaluation considered PTC, LFR, and CPC technologies according to the following criteria:

- Performance: efficiency under target operating conditions and energy yield per unit area.
- Feasibility: assembly complexity, availability of local components, and degree of national design participation.
- Operation: safety, maintenance requirements, and operational simplicity.

The analysis showed that, although PTC and LFR systems offer higher peak performance, they require specialized components and tracking systems that increase system complexity. The CPC was therefore selected as a more balanced solution, providing adequate thermal performance within the target range while enabling simpler assembly, reduced dependence on imported components, and lower operational risks, such as avoiding the need for defocusing during stagnation events.

The selection of CPC technology is further supported by recent studies demonstrating its versatility for solar heat applications, spanning a wide range of configurations and performance levels. Experimental and numerical works have explored CPC systems using thermosiphoning and nanofluids, optimized geometries, and hybrid working fluids, achieving temperature ranges from below 100°C up to 300°C and efficiency improvements under specific conditions (e.g., [14–17]). Other contributions have focused on advanced optical characterization, such as the dynamic concentration factor for CPC evaluation [18], or on large-scale implementations, such as external CPC arrays delivering process heat in the 70–170°C range with competitive costs [19].

Despite these advances, most reported systems operate without integrated thermal energy storage, limiting their ability to provide dispatchable heat for industrial applications. In this context, the present work differs from most previous studies by targeting the 100–150°C range with a CPC-based system coupled to a concrete thermal energy storage unit, enabling improved operational flexibility while maintaining a design oriented toward local manufacturability and cost-effectiveness.

Thermal energy storage

The integration of thermal energy storage (TES) is essential for industrial solar thermal systems, as it decouples heat generation from demand, enabling more stable operation and improving dispatchability.

Conventional mid-temperature solutions, such as pressurized water tanks or thermal oil systems, significantly increase capital costs due to the requirement for high-pressure vessels. Consequently, this work focuses on concrete-based TES as a more viable and cost-effective alternative. Sensible heat storage in concrete is a mature technology that has been demonstrated in power generation applications [20–23]. These systems typically consist of an array of tubes embedded within a concrete block. During the charging process, a hot fluid circulates through the tubes, transferring heat to the solid medium, while during discharge, the solid medium delivers heat to the circulating fluid.

The selection of concrete for the prototype design is based on several advantages: (i) local manufacturability, leveraging existing expertise in civil engineering and materials; (ii) cost-effectiveness, due to low material costs and the potential for modular prefabrication; and (iii) versatility, as it can accommodate a wide range of heat transfer fluids and pressurized cycles more effectively than large storage tanks.

Recent review studies [24,25] summarize advances in concrete-based thermal storage, generally focused on higher temperature ranges than those considered in this work. These studies highlight key challenges related to fabrication techniques, material formulation, and system design, which directly affect construction feasibility and thermal performance. They also report both experimental methods for property characterization and numerical approaches for evaluating

[1] Preliminary viability threshold of 500 USD/m^2 is obtained by adapting a previous analysis [12], which compared the economic viability of solar concentrating technologies for complementing fossil fuel in industrial heat in Uruguay.

thermal behavior.

Within this context, the present work addresses key design-stage challenges of the concrete-based TES system developed for the project pilot plant. These include the low thermal conductivity of concrete—explored through different formulations and additives and supported by preliminary experimental characterization of thermal conductivity— as well as the definition of storage geometry to meet power and capacity requirements under cost constraints. The transient thermal behavior during charging and the resulting thermal stratification are also analyzed. Since the TES unit has not yet been constructed, the reported results are limited to design studies, material characterization, and numerical simulations. Experimental validation of the complete storage system, including long-term performance, remains future work.

Scope and objectives

Despite significant advances in CPC-based collectors and thermal energy storage (TES), most studies focus on individual components or on isolated methodological approaches (e.g., numerical or experimental). Integrated collector–storage designs at pilot scale, addressing realistic operating conditions from a system-level perspective, remain relatively scarce. This gap limits the translation of component-level knowledge into practical engineering solutions for industrial heat supply.

In this context, this work presents the early-stage development of a pilot SHIP system from a system-level perspective, targeting representative industrial heat demand conditions. The focus is on engineering design, component integration, and preliminary validation through a combination of analytical models, numerical simulations, and experimental results. Detailed system operation and techno-economic assessment are beyond the scope of this study.

The paper describes the design and anticipated operation of a pilot plant currently under construction. While no full-system tests are reported, a first CPC collector prototype has been designed, fabricated, and experimentally characterized. For the thermal energy storage component, the design methodology, first-stage material characterization, and numerical performance assessment are presented; however, experimental validation of the complete TES unit remains future work. Component sizing, control strategies, and safety considerations are presented as design outcomes supported by standard engineering methods and supplier data. Discrepancies between model predictions and experimental results are analyzed to identify key limitations and guide design improvements.

The main contributions of this work are:

- An integrated methodology for CPC collector design and analysis, combining ray-tracing, thermal modeling, and experimental testing to identify dominant loss mechanisms and key design parameters.
- Experimental–numerical evaluation of reflector materials, linking spectral reflectance measurements with ray-tracing simulations to assess the role of specular and diffuse components under CPC geometry.
- Design and initial assessment methodology for a concrete-based TES prototype, based on a two-stage approach (analytical pre-dimensioning and transient numerical modeling), supporting its application in mid-temperature systems.
- System-level design framework for pilot-scale SHIP systems, integrating collectors, storage, and hydraulic/control subsystems to meet representative industrial heat demand conditions under realistic operating constraints.

The remainder of the paper is organized as follows. Section 2 describes the system design methodology, modeling approaches, and experimental procedures. Section 3 presents the main results, including collector performance and TES evaluation. Section 4 summarizes the conclusions and outlines future work toward full system operation and validation.

Materials & methods

This section presents the modeling framework and the initial experimental activities that support the design and evaluation of the system components. Numerical modeling is applied to support component sizing, performance prediction, and sensitivity analysis. Simplified models are developed for the main system components (solar collectors, thermal storage, heat dissipator, and piping), focusing on the dominant design parameters. These models build on previous developments by the academic team and are complemented by dedicated formulations for the concrete accumulator and the solar collectors. These simplified models are validated against more detailed numerical simulations using advanced tools such as OpenFOAM and Tonatiuh, complemented by in-house developments.

Rather than applying these tools in isolation, this work adopts an integrated approach that combines simplified models, state-of-the-art numerical simulations, and experimental activities within a consistent design framework. This integration links system-level design decisions with detailed component behavior, while the combined use of advanced simulations and targeted experiments enables both the validation of model predictions and the identification of key design parameters and performance limitations. This integrated approach is particularly valuable for the analysis and design of the main system components, namely the solar collector and the thermal energy storage system, under realistic operating conditions.

The detailed development of the models and experimental methodologies for each component has been presented in previous works within the framework of SWC 2025 [26–28]. In this article, only the key aspects are summarized to provide a coherent overview of the pilot plant design. The reader is referred to those contributions for a more comprehensive description of the modeling approaches and experimental procedures.

In the first subsection (2.1), the overall system design methodology is described, including the installation layout, operating modes, fluid circuit conditions, and the design and selection criteria for the main system components, such as the cooling heat exchanger, piping, expansion system, control devices, and instrumentation. Subsection 2.2 describes the methodology adopted for the design, manufacturing, and testing of the solar collector, while Subsection 2.3 describes the design methodology and experimental procedures associated with the thermal energy storage system. Since the pilot plant is currently under construction, the results presented in this work combine design studies, numerical analyses, and component-level experimental characterization, while full-system validation remains future work.

Pilot plant design and operating modes

A schematic of the proposed system and its operating modes is presented in Fig. 1. It integrates an array of compound parabolic concentrator (CPC) collectors with vacuum tubes for solar heat capture, and a modular concrete-based thermal energy storage module with embedded metallic piping, where each component is connected through a closed-loop primary fluid circuit.

The conceptual facility is intended to operate in five main modes:

- Direct production: the working fluid carries heat from solar collectors directly to the industrial process when useful power is lower than (or equal to) heat demand.
- Storage (charge): useful heat is directed to the concrete thermal storage unit for later use.
- Indirect production (discharge): process heat is supplied from the thermal storage during low-solar periods.
- Parallel (surplus; shown in Fig. 1): collectors simultaneously supply both the process and the storage when heat generation exceeds demand.

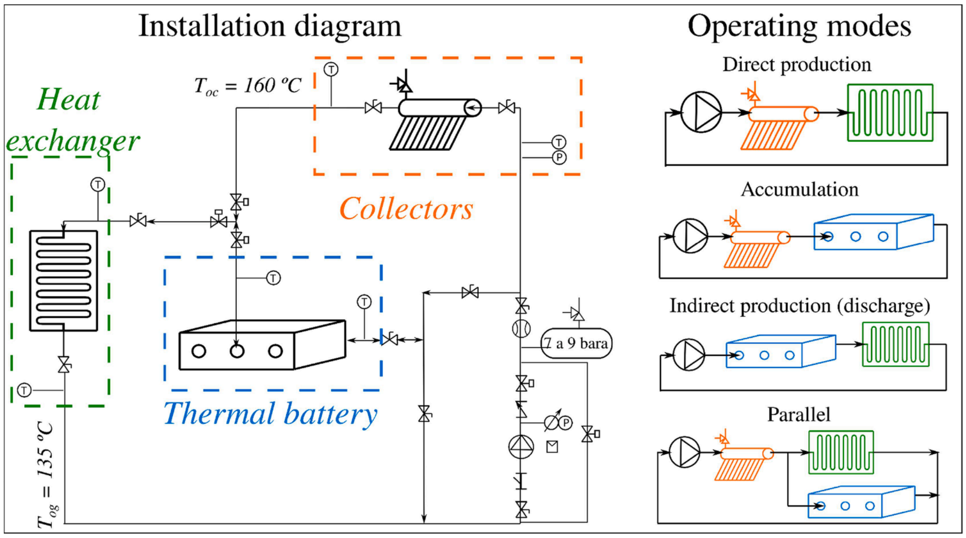

Fig. 1. Schematic diagram of the solar thermal pilot plant and operating modes.

- Parallel (compensation, not shown in Fig. 1): collectors and TES jointly supply the process heat demand.

The system is designed to deliver a nominal thermal power of about 10 kW under reference conditions: irradiance G_{hem} = 1000 W·m^{-2}, ambient temperature T_a = 20°C, and mean fluid temperature $T_f \approx$ 145°C. The selection of operating conditions is guided by combined thermal and pressure constraints, including limits on maximum temperature, the need to maintain a sufficient temperature difference for sensible heat storage, the requirement to emulate representative industrial heat demand, and typical pressure ratings of industrial components. Accordingly, nominal primary-loop temperatures are set to 160°C at the collector outlet and 135°C at the process outlet, corresponding to steam generation at approximately 130°C, while the system is designed to operate at a nominal pressure of 7 bara with a maximum allowable pressure of about 10 bara. These operating conditions provide a consistent basis for component sizing and integration, ensuring coherent operation under a common set of requirements. The design methodology and the steps followed are presented in the following sections.

Dimensioning of collector field and cooling heat exchanger, and expected performance

The useful power produced by the collector, denoted as $\dot{Q}_u$, is defined according to the thermodynamic model presented in the ISO 9806 (2025) standard [29] for glazed collectors as follows:

$$\frac{\dot{Q}_u}{A} = \eta_{0,b}[K_b G_b + K_d G_d] - a_1(T_f - T_a) - a_2(T_f - T_a)^2 - a_5\frac{dT_f}{dt} \quad (1)$$

The terms G_b and G_d represent the direct and diffuse solar irradiance on the collector plane. The variable T_f is the mean fluid temperature (average of inlet and outlet), and T_a is the ambient temperature. The collector performance is described by the parameters $\eta_{0,b}$, K_b, K_d, a_1, a_2, and a_5. The parameter $\eta_{0,b}$ is the peak efficiency at normal incidence for direct irradiance. The coefficients a_1 and a_2 represent thermal losses. The parameter a_5 corresponds to the effective thermal capacity divided by the aperture collector area (A). The factors K_b and K_d describe the incident angle modifier (IAM) for direct and diffuse irradiance, respectively. All parameters are constant except K_b, which depends on the incidence angle of the direct beam, θ. For convenience, the aperture area is used as the reference instead of the gross area specified in the standard. By dividing this equation by the global hemispherical solar irradiance on the collector plane (G_{hem}), and assuming normal incidence (K_b = 1), clear-sky conditions (diffuse fraction of 15%), and steady-state conditions ($dT_f/dt = 0$), the collector efficiency can be expressed as:

$$\eta = \eta_{0,hem} - a_1\frac{T_f - T_a}{G_{hem}} - a_2\frac{(T_f - T_a)^2}{G_{hem}} \quad (2)$$

Where $\eta_{0,hem}$ is the peak efficiency at normal incidence referred to the global hemispherical solar irradiance, which is estimated as $\eta_{0,hem} = \eta_{0,b} \cdot (0.85 + 0.15\,K_d)$.

The sizing of the collector field is based on the assumption that the field behaves similarly to a single collector. The system is designed to deliver a nominal thermal power of about 10 kW under reference conditions defined above. The initial design performance parameters were estimated from commercially available CPC data and supplier literature [30,31]: peak efficiency $\eta_{0,hem} \approx 0.55$, linear heat loss coefficient $a_1 \approx$ 1.3 W·m^{-2}·K^{-1}, and negligible quadratic heat loss term $a_2 \approx 0$ W·m^{-2}·K^{-2}. Under these conditions (T_f = 145°C and T_a = 20°C), the estimated collector efficiency using Eq. (2) is about 38%, which leads to a required aperture area of approximately 26 m^2 to achieve $\dot{Q}_u \approx$ 10 kW. Using the selected ΔT = 25°C, the resulting volumetric flow rate is estimated from the energy balance.

The primary heat transfer loop is designed to operate with a pressurized liquid-phase working fluid (water mixed with 30% glycol) maintained in a subcooled liquid state at elevated temperatures to avoid steam formation and to simplify compliance with local regulations for steam systems. Given the objective of supplying heat that emulates steam-generation loads for industrial processes, and considering typical maximum temperatures for CPC systems (~150°C), the system is designed to emulate steam production at roughly 130°C (≈ 2.7 bara equivalent) at the process interface. A design temperature rise across the collector field of 25°C (e.g., from 135°C at the inlet to 160°C at the outlet) is adopted; under these assumptions, the nominal volumetric flow rate for the primary loop is on the order of 6.4 L·min^{-1}.

To reproduce industrial steam demand in a controlled and safe manner, a cooling vessel consisting of a water tank with an internal coil is selected (the primary circuit is inside the coil; the secondary side is saturated water/steam in the tank). The primary fluid circulating through the coil transfers heat to the tank water, which can then produce steam at approximately 1–1.5 bara (100–110°C). The water tank–coil arrangement is adopted because it provides a simple and robust interface to emulate steam generation while keeping peak pressures low for safety and regulatory reasons.

The cooling coil length is determined using the ε–NTU approach [32], assuming a nearly infinite heat capacity rate for the secondary fluid ($C_r \approx 0$), which is considered to be boiling at 110°C. It is further assumed that the cooling coil removes the nominal thermal power under design conditions (10 kW, flow rate of 6.4 L·min^{-1}, cooling from 160°C to 135°C).

A bypass segment with a controllable valve allows part of the primary fluid to bypass the cooling vessel, enabling temperature regulation and variation of the consumption profile. The selected coil length is 3.36 m, with 20% of the primary fluid bypassing the cooling vessel under the reference conditions described above. To predict behavior at off-design flow rates, the model applies NTU scaling with primary-side velocity dependence, following a power-law derived from Dittus–Boelter correlations (local $U \propto v^{0.8}$).

Table 1 summarizes predicted combinations of collector and cooling-vessel performance for several irradiance levels at $T_a = 20$°C. The collector outlet temperature (T_{oc}, equal to the cooling-vessel inlet temperature) is assumed to be actively controlled (via pump speed modulation) at 160°C. The cooling coil outlet temperature (T_{og}), solar field efficiency (η), and resulting volumetric flow rate ($\dot{V}$) are calculated. The total heat power produced by the solar field ($\dot{Q}_u$) is assumed to be equal to that delivered to the cooling coil, neglecting piping heat losses. Preliminary results indicate that, under expected operating conditions, irradiance values down to ~500 W·m^{-2} can still produce outlet temperatures compatible with the process-emulation target ($T_{og} > 130$°C), which represents a practical lower operating limit for the proposed configuration.

Working fluid circuit design and safety considerations

Component selection and circuit layout were established in accordance with standard engineering practices for pressurized liquid heating systems, taking into account applicable codes and local regulations (e.g., [33,34]). The system is designed to operate with a 30% propylene glycol–water mixture (selected to provide freeze protection and to ensure the liquid remains subcooled at the highest design temperature). The saturation temperature of the chosen mixture at the design working pressures (7–8 bara) is sufficiently above the operating range (>185°C), ensuring that the primary loop remains in the liquid phase during normal operation.

Key design pressures adopted for component selection were a nominal design pressure of 7 bara and a maximum allowable pressure of 10 bara. These values are selected to be compatible with the lowest-rated component expected to be used and to provide a reasonable safety margin.

Pumps, flowmeter and piping. Pump selection was driven by the highest anticipated circuit pressure drop (worst-case mode). A centrifugal pump equipped with a variable-frequency drive (VFD) is selected conceptually to allow flow modulation and accommodate a wide range of test conditions. A turbine-type flowmeter is selected for its suitability at the low flow rates and elevated temperatures expected; however, preliminary sizing indicates that the flowmeter is a significant contributor to hydraulic resistance in the pilot plant loop. A bypass around the pump is included in the layout to enable pump operation at higher nominal speeds during system filling or testing, while regulating the working flow through a control valve.

Preliminary hydraulic resistance estimates were calculated using standard correlations and handbook data [35], together with manufacturer pressure–flow curves. The longest piping run between components was estimated at ~ 25 m; a ½″ diameter pipe is selected in the preliminary design to keep mean fluid velocities below ~ 1 m·s^{-1} (≈ 0.57 m·s^{-1} at nominal flow), balancing pressure drop, material availability, and insulation cost. A 75 mm mineral wool insulation layer is included in the thermal-loss budget, resulting in estimated steady heat losses of ≈ 400 W at mean fluid temperatures near 145°C and an ambient temperature of 20°C (≈ 4% of the nominal 10 kW output; this fraction increases at lower irradiance).

Table 1
Results of estimated operation conditions of the system, combining solar field and emulated steam generation.

G (W/m^2)	T_{oc} (°C)	T_a (°C)	T_{og} (°C)	η (%)	$\dot{Q}_u$ (kW)	$\dot{V}$ (L/min)
1000	160	20	135.4	38.4	9.98	6.36
750	160	20	133.6	33.0	6.44	3.82
500	160	20	130.3	22.5	2.92	1.54

Expansion vessel concept and thermal coupling. Because stagnation conditions (no flow, available radiation) are inevitable, an expansion vessel is included. The expansion vessel is sized assuming a design pressure of 7 bara and a maximum operating pressure of 10 bara, limited by the nominal pressure of the circuit components (11 bara). The calculation follows the standard methodology for solar thermal system expansion vessels [36], adapted to the higher pressures and temperatures of the present installation. Since the standard approach does not explicitly consider the final gas temperature inside the vessel, an iterative procedure is implemented, taking into account the limitations of commercially available vessels (maximum pressure 11 bara, maximum temperature 100°C) and the supplier restriction that the pre-charge pressure must not exceed half of the maximum allowable pressure. Accordingly, the cold pre-charge pressure is set to 5 bara.

The total installation volume, including piping, collector manifolds and storage unit, is estimated at 60 L, and a thermal expansion coefficient of 0.1 is adopted for a 30% water–glycol mixture between 20°C and 150°C. A vaporization volume of 11.4 L is calculated from the collector manifolds and vertical risers. The vessel is sized iteratively using the ideal gas law to predict the final pressure during stagnation. The analysis assumes a vessel water temperature below 40°C (before the stagnation event) and an injected fluid temperature of 140°C in the event of manifold vaporization. The final temperature is obtained from an energy balance of the mixed water masses, allowing determination of the final gas volume and pressure.

The results indicate that a nominal volume of 125 L satisfies the design limits, leading to a final pressure of about 10 bara during stagnation. However, a 150 L vessel is selected due to market availability, resulting in a maximum pressure of 9.6 bara and providing additional margin for future expansion of the solar field.

To limit the vessel temperature to below 40°C during normal operation, the connection between the main circuit and the expansion vessel is designed as an uninsulated short length of pipe, allowing conduction and free convection to the ambient to reduce the temperature of the fluid in the vessel. A conservative fin/pipe heat-transfer model (adiabatic-tip, infinite-fin approximation) is used to size the connection length and verify that heat gains to the vessel remain small under worst-case ambient conditions. To account for heat transfer through both the pipe wall and the stagnant internal fluid, an effective pipe–fluid thermal conductivity of 23.5 W/m·K is adopted. The calculations indicate very small heat transfer through this connecting line (on the order of 5–12 W under conservative assumptions), supporting the validity of the approach for maintaining vessel temperatures below 40°C under operating conditions.

Measurement, monitoring and control. The preliminary instrumentation plan includes PT-100 class sensors at the inlet/outlet of the collector field, the cooling vessel coil, and within the thermal storage blocks. Additional sensors are planned for the secondary (tank) side to monitor saturated-water/steam conditions. Pressure transducers are specified for the solar-field outlet and the cooling vessel; additional manometers are included for commissioning and safety checks.

Flow measurement (turbine meter), with a stated accuracy of approximately 1% in the 1–10 L·min^{-1} range, is used to enable reliable energy calculations together with temperature measurements, from which instantaneous thermal power and accumulated energy can be derived. A small meteorological station (plane-of-array irradiance, global and diffuse horizontal irradiance, and ambient temperature) is included in the instrumentation list to enable solar-to-thermal performance calculations for both the collector field and the overall system.

A PLC-based control scheme is proposed to implement pump-speed modulation for collector outlet temperature control (e.g., setpoint of 160°C for baseline tests), solenoid-actuated steam venting from the cooling vessel to regulate internal pressure and temperature, and logic for switching between operating modes (direct, storage, discharge, parallel). All data will be recorded to a data-acquisition system for post-processing and performance assessment during experimental campaigns once the pilot plant is operational.

Operating modes are initially set manually through different valve configurations; future versions of the plant design could include automatic switching between operating modes as a function of irradiance, heat demand, and system temperatures. Although the operating modes shown in Fig. 1 allow evaluation of a range of heat-demand scenarios and environmental conditions (e.g., heat demand higher or lower than the heat produced by the collectors, with the possibility of storing or releasing accumulated heat), the simplicity of the cooling device designed for the test facility may limit the range of industrial heat-demand scenarios that can be reproduced under real operating conditions. In particular, the capability of the system to represent variable heat-demand profiles, transient start-up and shutdown conditions, and interaction with return flows from the emulated industrial process has not yet been fully assessed.

Up to this point, the design of the system components follows standard engineering practice, with only minor adaptations (e.g., for expansion vessel sizing). By contrast, the solar collector and the thermal energy storage (TES) unit require a more detailed design methodology, which is presented in the following sections through a combination of simplified models, detailed numerical simulations, and experimental activities. This reflects the limited availability of standardized design procedures and commercially mature solutions in the local context, particularly for the TES system.

Methodology for solar collector field design, manufacturing and testing

A non-tracking CPC collector field is proposed to ensure operational simplicity and low maintenance costs in industrial environments. The first prototype features a concentration ratio (CR) of approximately one to maximize the acceptance angle, ensuring consistent solar energy collection throughout the day without moving parts. The design choice is motivated by the performance of low-concentration commercial collectors (CR<1), whose thermal efficiencies at temperatures near 145 °C are expected to be between 30% and 45% [30,31][2]. By optimizing the concentration profile and minimizing thermal losses, the current design aims to achieve the 38% target efficiency established in previous sections.

As illustrated in Fig. 2, the system integrates evacuated tube collectors (ETC) with heat pipe (HP) technology. This configuration takes advantage of the widespread availability of commercial evacuated tubes while achieving high thermal performance at elevated temperatures. The collector uses standard absorber tubes, whereas the manifold, casing, reflectors, and support structure are custom-designed for local manufacturing. Fig. 2 (left) depicts the cross-section of the evacuated tube and the reflector geometry, illustrating incident radiation interactions. Fig. 2 (right) shows a schematic of the manifold section, detailing the heat pipe integration and various fin configurations (single and double-fin arrangements) for enhanced heat transfer.

In this system, once solar radiation is captured by the absorber surface (inner tube), its temperature increases and heat is transferred to the working fluid via heat pipes. The heat pipes act as high-conductance thermal bridges, with effective thermal conductivities reaching orders of magnitude higher than solid copper [37]. A significant operational advantage of this "dry-connection" design is the ability to replace individual tubes in the event of failure without requiring a full system shutdown. The selected evacuated tubes have an outer diameter of 58 mm and an inner tube diameter of 47 mm, with a glass thickness of 1.6 mm and an active evaporator length of 1715 mm. Including the adiabatic section, condenser, and manifold insulation, the total unit length is approximately 2 m.

The selective absorber surface is located on the outer surface of the inner tube (47 mm diam.) with 93% absorptance and 5% emittance, based on manufacturer datasheets. The glass cover provides a high transmittance of 88%, resulting in a typical design transmittance-absorptance product near 0.8. Based on a technical datasheet of locally available ETC collectors [30], the stagnation temperature is expected to exceed 230°C, providing a wide safety margin for the target 100–150°C range. Additionally, the design incorporates a tilt correction system to ensure a minimum inclination of 20° facing north, a physical requirement for proper gravity-assisted operation of the heat pipes.

Thermal insulation in the manifold is designed to limit thermal losses to approximately 2% of the nominal power (≈200 W) for fluid and ambient temperatures of 145°C and 20°C, respectively. A 150 mm layer of glass wool is required to meet this target.

To optimize both optical and thermal efficiency, a combination of modeling approaches and experimental tests is used. Ray-tracing simulations combined with experimental reflectivity measurements are used to evaluate optical performance, while thermal modeling is developed to assess heat-transfer behavior. These results are compared with experimental thermal performance characterization of solar collectors performed in a solar collector test bench.

Optical design and reflector geometry

To capture both beam and diffuse radiation without tracking, and given the design constraint of CR = 1, an involute reflector profile is adopted (Fig. 2, left). Under ideal optical conditions, this geometry directs all incident rays onto the absorber surface, independently of their angle of incidence within a 90° acceptance range. This requirement inherently limits the maximum concentration ratio to unity ($CR_{max} = 1$), as the involute must remain perpendicular to the tangents of the cylindrical absorber [38].

For the first prototype, considering local availability, cost, and expected durability, reflective sheets of commercially polished stainless steel (CPSS) from the AISI 300 or 400 series are proposed, with a thickness range of 0.5–0.8 mm. Stainless steel is known for its durability even outdoors and, unlike other reflective materials, CPSS is available in the Uruguayan market. However, comparison of the optical properties of CPSS and other reflective surfaces is also presented in further sections.

Optical performance is analyzed using Tonatiuh [39], an open-source software based on the Monte Carlo ray-tracing method, which allows accounting for both specular and diffuse surface reflectance, both of which are expected to be relevant due to the short distance between the reflector and the absorber. By analyzing the ratio of rays incident on (and absorbed by) the absorber surface to the total rays arriving at the aperture area, optical efficiency can be determined. This is performed for normal incidence and also for various transversal (θ_T) and longitudinal (θ_L) incidence angles.

Thermal modeling

The thermal performance of the system is evaluated through a model that accounts for the total thermal resistance from the absorber to the working fluid, as schematized in the electrical analogy of Fig. 3. Heat is conducted from the absorber surface (8) through aluminum fins (10) to the HP evaporator (9), where the numbers correspond to those in Fig. 2. The design considers vacuum tube configurations with one or two fins, where a second fin improves heat transfer at a higher cost. From the

[2] These values are highly uncertain, due to being estimated from efficiency curves which are obtained from tests at lower temperatures.

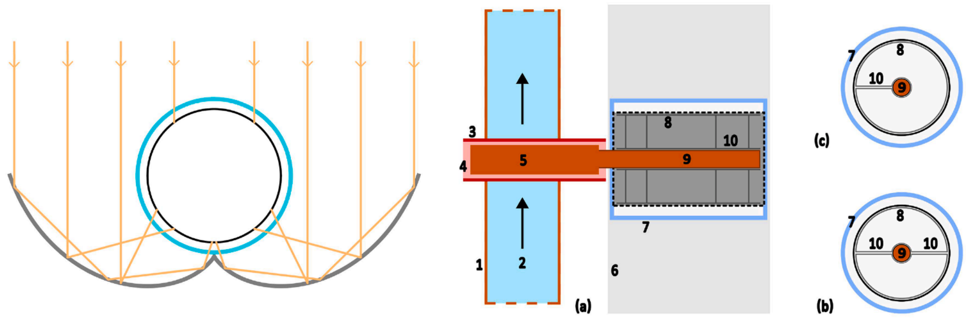

Fig. 2. Left: Cross section of evacuated tube and reflector geometry, indicating normal incident radiation and interactions. Right:. Scheme of a section of the manifold with one HP and a vacuum tube. a) Front view of the system. b) Cross-section view of a VT with one fin. c) Cross-section view of a VT with two fins. 1-Manifold. 2-Working fluid. 3-Socket. 4-Thermal paste. 5-HP condenser. 6-Reflective plate. 7-Vacuum tube. 8-Absorber. 9-HP evaporator. 10-Aluminium fins.

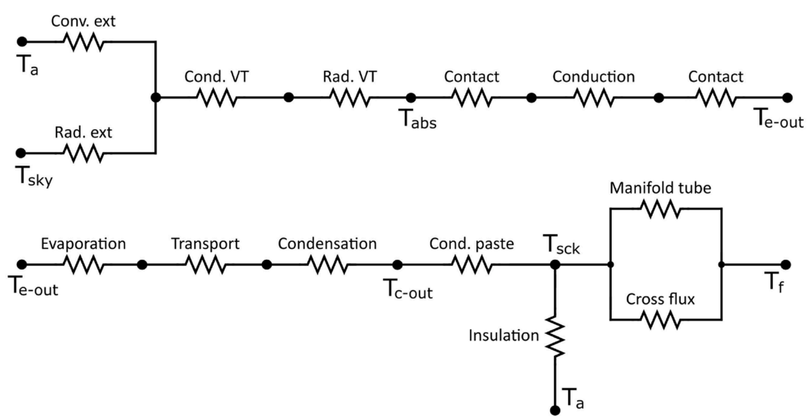

Fig. 3. Electrical equivalent diagram of the temperatures and thermal resistances of the system. Temperature nodes: Ta - ambient; T_{sky} - sky; T_f - fluid; T_{abs} - absorber surface; $T_{e\text{-}out}$ - evaporator external surface; $T_{c\text{-}out}$ - condenser external surface; T_{sck} - copper socket welded to the manifold.

condenser (5), heat crosses a layer of thermal paste (4) to reach the copper socket (3) welded to the manifold (1), where it is finally transferred to the fluid through forced convection (either directly through the socket wall or through the manifold pipe wall by a fin-like mechanism).

With the developed thermal model, whose formulation and validation are presented in another work [26], node temperatures are calculated for a range of working fluid temperatures, assuming an ambient temperature of 20°C and typical clear-sky irradiance conditions ($G_b = 850$ W/m^2, $G_d = 150$ W/m^2). The model predicts the useful heat output, thermal losses, and overall system efficiency. To maximize efficiency, the absorber temperature must be minimized for a given heat flux, which is accomplished by minimizing the thermal resistances in the heat path.

The manifold design (main diameters, pipe, and socket thicknesses) is supported by the model. Through a detailed 2D thermal analysis that considers conduction heat transfer within the manifold sockets and pipe wall, as well as convection between the water socket and manifold inner surfaces, the corresponding thermal resistances are determined.

Furthermore, a sensitivity analysis is performed for the main parameters of the system, including flow rate, thermal paste used, and the number and thickness of the internal aluminum fins (which were found to vary across fin configurations for locally available heat pipe evacuated tubes).

Experimental test methods

Four different materials were studied as potential reflectors to evaluate their performance and durability, including commercially polished stainless steel from the AISI 300 or 400 series, pristine and aged commercial polished aluminum, and high-reflectivity aluminum specifically designed for solar applications. The spectral reflectance of these materials was measured using an Ocean Optics S2000 spectrometer and an Ocean Optics ISP-REF integrating sphere, providing the optical properties required for the subsequent ray-tracing simulations and performance models. Total and diffuse reflectance were measured, and specular reflectance was obtained as the difference between the two. To incorporate these results into ray-tracing simulations, a methodology was developed to convert experimental test results into total reflectance and surface roughness values.

For evaluating the thermal performance of the solar collectors, the Solar Water Heater Test Bench (BECS, for its name in Spanish) at the Solar Energy Laboratory of Universidad de la República (Salto, Uruguay) is used. Experimental procedures follow the ISO 9806:2025 [29] standard and include both steady-state and quasi-dynamic testing conditions. Although the current facility limits active testing to a maximum fluid temperature of 100°C, the results allow for a reliable extrapolation of the efficiency curve up to approximately 130°C with acceptable uncertainty. This range is sufficient to characterize the optical efficiency and the primary thermal loss coefficients. First, a modified commercial CPC-ETC collector was tested for model calibration [Rodríguez-Muñoz et al., in press]. Subsequently, a first prototype of the designed and manufactured CPC-ETC collector was also tested, and its results are presented in this work.

Once the pilot plant is operational, in situ performance tests at higher operating temperatures are planned.

First prototype characteristics and fabrication methods

The prototype design is derived from the methodology described above and represents a first iteration aimed at experimentally evaluating the design and identifying opportunities for improvement. The collector module consists of 15 heat pipes with a stainless steel reflector and a concentration ratio of CR ≈ 1, resulting in a total width of 2.25 m and an aperture area of 3.9 m^2. This configuration is selected to comply with size constraints of the BECS test bench.

The complete collector field consists of six such modules, resulting in a total aperture area of approximately 24 m^2, consistent with the target thermal power of ~10 kW defined in Section 2.1.

The reflector geometry was fabricated using a CNC press brake, with a planned transition to stamping dies to eliminate faceting and ensure a continuous optical profile. The manifold is constructed from copper using CNC laser cutting and welding, while the support structure is made of 1.5–2 mm galvanized steel.

Fig. 4 (left) shows the fabricated copper manifold, while the right panel presents the assembled prototype mounted in the BECS facility for experimental testing.

Thermal energy storage design methodology

The selected TES unit consists of a concrete-based solid–fluid heat exchanger, in which water flows through an array of tubes embedded in a concrete matrix, similar to configurations reported in the literature [20,21,23,40]. The storage unit is designed as a block-type accumulator operating under alternating charge and discharge phases: during charging, a high-temperature working fluid heats the concrete matrix, while during discharge, the stored heat in the concrete is transferred back to the fluid.

Carbon steel was selected as the pipe material due to its proven chemical and mechanical compatibility with concrete, ensuring structural integrity under repeated thermal cycling. Laboratory testing was conducted to determine the thermal conductivity of candidate concrete formulations, supporting the selection of suitable mixtures [20,21]. Accordingly, the concrete composition and the thermal design of the storage unit are addressed as key aspects in this section, as they directly determine the overall system performance.

The design process is described in greater detail in a companion study [27], where the thermal aspects and methodology are further elaborated, and additional factors such as construction costs and hydraulic resistance are also considered.

Initial dimensioning: analytical approach

The maximum thermal capacity of the storage unit, E_{max}, is given by the combined thermal capacity of concrete, steel, and confined water. Since the mass of the concrete matrix is significantly larger than that of the steel and water, the storage capacity is primarily governed by the concrete mass and the operational temperature range. Thus, it can be approximated as:

$$E_{max} \approx m\ c\ (T_{max} - T_{min})$$

where m and c are the concrete mass and specific heat, respectively, and T_{max} and T_{min} are the maximum and minimum storage temperatures. Consistent with the operating conditions defined in Section 2.1, these values are taken as the nominal collector field outlet temperature (T_{oc}) and the nominal process-side cooling coil outlet temperature (T_{og}), respectively.

As these temperatures are constrained by the system operating conditions (Section 2.1), the required concrete mass is determined by the target storage capacity. A 3-hour storage duration at nominal power (10 kW, consistent with the solar field) corresponds to 30 kWh, which, for $T_{min} = 135°C$ and $T_{max} = 160°C$, yields a minimum concrete volume of approximately 2 m^3.[3]

Since the TES operates under transient conditions, conventional steady-state formulations for recuperative heat exchangers are not directly applicable. Nevertheless, an initial sizing is performed using a simplified recuperative heat exchanger model with several assumptions. Accordingly, a two-step design methodology is adopted: first, a preliminary design is obtained using the simplified model; second, this design is refined through numerical simulations of heat transfer within the TES, leading to the final configuration.

The analytical approach assumes that, although both fluid and solid temperatures vary with time, their axial profiles evolve while maintaining a nearly constant mean temperature difference ΔT_{mean}. Under this assumption, the mean heat transfer rate is given by:

$$\dot{Q}_{st} = (UA)_{st} \Delta T_{mean}$$

Where $(UA)_{st}$ is the product of the overall heat transfer coefficient and the heat transfer area. The estimation of U includes the internal convective heat transfer coefficient, conductive resistance of the pipe walls, and an equivalent resistance of the thermally affected concrete, modeled as steady-state radial conduction.

To evaluate alternative configurations, mean temperature differences of 3°C to 10°C (i.e., 12–40% of the total temperature span) were assumed. For a design heat transfer rate of 10 kW, this results in $(UA)_{st}$ values between 1000 and 3300 W/K. Assuming an internal convective coefficient of 2000 W/m^2K and a concrete thermal conductivity of 2 W/mK, the resulting overall heat transfer coefficient ranges between 180 and 320 W/m^2K. Consequently, the required heat transfer area (pipe surface) is estimated to be between 3 and 19 m^2, depending on the assumed ΔT_{mean}.

Based on these results, a reference heat transfer area of 12 m^2 is selected as the starting point for the detailed design. Exploring pipe diameters (1/8″ to 3/4″) and fluid velocity ranges yields configurations with 1 to 6 tubes and total pipe lengths ranging from 150 to 350 m. The final geometry is determined based on numerical modeling results, including pressure drop and assembly cost considerations.

Fine-tuned dimensioning and performance evaluation: numerical modeling

The detailed thermal design of the storage unit is based on evaluating the performance of different configurations by varying the number, length, thickness, and diameter of the pipes. The numerical model is implemented in OpenFOAM [41] using the *chtMultiRegionFoam* solver, solving the heat equation in both solid and fluid regions. Simulations are performed under a constant flow rate of 6.36 L/min, with an inlet temperature of 160°C during a 3-hour charging period, and a uniform initial temperature of 135°C.

To reduce computational cost, the fluid domain inside the pipes is discretized only along the axial direction, assuming cylindrical symmetry, while the solid concrete domain is fully discretized in three dimensions. The mesh configuration and domain regions (water, steel pipe, and concrete) are illustrated in the cross-section shown in Fig. 5.

To assess thermal stratification, total stored energy, and charging rates, the numerical results are analyzed in terms of temperature distribution and state of charge (SOC). The temperature field during the charging stage is characterized using the dimensionless temperature difference, θ^*, defined as:

$$\theta^* = (T - T_{ini}) \ / \ (T_{max} - T_{ini}) \tag{3}$$

where T_{ini} is the initial temperature. The SOC of the thermal battery is evaluated using:

$$SOC = E / E_{max} \tag{4}$$

with

$$E = \sum_i \left[\int_{V_i} \rho_i C_{p,i} (T - T_{min}) dV \right] \tag{5}$$

where both the current stored energy, E, and the maximum storage

[3] Note that TES capacity is slightly larger than estimated as heat is also stored in the confined water and steel pipes.

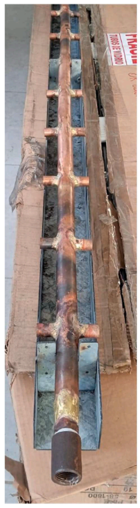

Fig. 4. Left: fabricated manifold for the first collector prototype. Right: First collector prototype mounted in the BECS.

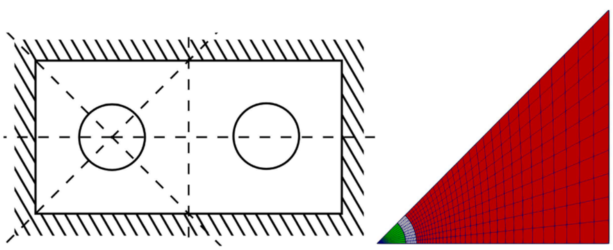

Fig. 5. CFD mesh cut of the simplified storage module geometry (green: fluid; gray: steel pipe; red: concrete).

capacity, E_{max}, include contributions from the concrete, steel, and water regions (index i indicating different regions). Thermal properties for each material are: $\rho = 2.50$ kg/l and $C_p = 0.80$ kJ/kg°C for concrete [25]; $\rho = 0.94$ kg/l and $C_p = 4.18$ kJ/kg°C for water-glycol mixture [42]; and $\rho = 7.85$ kg/l and $C_p = 0.49$ kJ/kg°C for steel [32]. Eq. (5) also provides the exact value of E_{max}, by substituting T_{max} in place of T.

In order to evaluate the mean temperature difference between fluid and concrete, ΔT_{mean} is determined by integrating T within concrete and fluid volumes:

$$\Delta T_{mean} = \frac{1}{V_f}\int_{V_f} TdV - \frac{1}{V_c}\int_{V_c} TdV = \overline{T}_f - \overline{T}_c \tag{6}$$

where f and c indicate fluid and concrete domains, respectively.

Concrete composition determination

The objective was to develop a concrete mix with a target thermal conductivity of approximately 2 W/m·K, using locally available materials while ensuring durability under thermal cycling and adequate resistance to fatigue and thermally induced cracking.

According to the literature, the thermal conductivity of concrete depends on the conductivity of the mortar and aggregates, the metallic fiber content (provided good interfacial bonding), and the moisture content, while it decreases with increasing temperature and porosity. In general, conductivity is largely governed by the aggregates: siliceous materials exhibit higher conductivity than calcareous ones, and since sand contains a significant fraction of quartz, an appropriate proportion of fines enhances thermal performance. Accordingly, granite aggregates with high silica content were selected to meet the target conductivity [43–45].

Previous studies indicate that, with good fiber–matrix adhesion, thermal conductivity is expected to increase approximately linearly with fiber content, as fibers act as thermal bridges. Hooked fibers are particularly suitable due to their improved bonding, while high compaction is required to achieve the desired performance [45–47].

Additional factors such as temperature, porosity, and moisture must also be considered. Thermal conductivity decreases with temperature; for instance, [45] proposed the empirical relation k=2.5−0.0034T, which suggests a reduction of approximately 20% at $T \sim 150$ °C. Porosity reduces conductivity, and excessive fiber content may hinder compaction. Therefore, achieving high compaction while maintaining a low water-to-cement ratio is critical, while increased moisture content generally enhances conductivity [43,47]. Moreover, if the base concrete exhibits low conductivity, the addition of fibers yields limited improvement; thus, the base mix must provide adequate performance.

Based on these considerations, an optimized mix design was defined, and the fiber content was varied between 0 and 250 kg/m^3 to assess its effect on thermal conductivity. The final formulation (Table 2) corresponds to a self-compacting concrete per cubic meter. A superplasticizer was incorporated to achieve high compaction and facilitate placement without the need for vibration.

Thermal conductivity evaluation

Accurate determination of thermal conductivity is essential for predicting the thermal behavior of the TES unit. It is measured according to ASTM D5334-14 [48]. This method is suitable for semi-infinite media, where the heat generated by the probe is fully absorbed by the surrounding material during the measurement.

Cylindrical specimens (10 cm radius and 20 cm length) with metallic fiber contents ranging from 0 to 250 kg/m^3 are tested. To accommodate the needle probe, axial holes (6 mm diameter and 7 cm length) are incorporated into the specimens during fabrication, accessible from both end faces. Measurements are conducted at room temperature using a TEMPOS RK-3 needle probe, suitable for thermal conductivity values in the range of 0.1 – 6.0 W/m·K [49]. Since thermal conductivity measurements exhibited limited repeatability, the reported values should be regarded as preliminary and further characterization of the thermal properties is planned as future work. To assess the implications of this uncertainty for the storage design, a sensitivity analysis is also performed over a representative range of conductivity values.

Results

This section presents the main results of the experimental and numerical analyses of the solar collector and thermal energy storage (TES)

Table 2
Concrete mix design for 1 m^3.

Item	Portland cement CPN 40	Fine sand	Coarse sand	Gravel 5-15	Superplasticizer	Water
Quantity (kg)	467.3	164.5	698.1	908.4	3.8	186.9

system described in Section 2, including comparison with model predictions to validate the proposed approaches and identify the dominant mechanisms governing system performance. The results are also used to refine component design.

Subsection 3.1 presents the performance assessment of the collector prototype, including optical characterization, ray-tracing simulations, thermal model calibration, sensitivity analysis, and experimental validation at BECS. Subsection 3.2 presents the TES design and analysis results, including thermal conductivity measurements and numerical performance evaluation leading to the final design.

Performance assessment of the solar collector

Optical design results: reflector materials and ray tracing

The results of the optical characterization of the reflector materials are summarized in Table 3. High-reflectance aluminum (HRAB) exhibits the highest total and specular reflectance, followed by commercial polished aluminum (CPA). The aged aluminum (ACPA) shows the third highest total reflectance but the lowest specular component, while commercial polished stainless steel (CPSS) presents the lowest total reflectance but higher specular reflectance than ACPA. These results highlight the significant impact of aging on polished aluminum surfaces, particularly through a reduction in specular reflectance and a corresponding increase in diffuse reflectance. The implications of these properties on collector performance are further analyzed through ray-tracing simulations (Table 3).

Ray-tracing simulations performed in Tonatiuh using 10^8 rays indicate that optical efficiency at normal incidence is less sensitive to differences in total reflectance than initially expected. This behavior is consistent with the collector geometry, as a significant fraction of the incident radiation reaches the absorber directly without interacting with the reflector. Consequently, the effect of reduced reflectance is partially mitigated. A comparison between CPSS and ACPA results further indicates that both specular and diffuse reflectance contribute to overall performance. This is likely due to the short distance between the reflector and absorber surfaces, which increases the probability of diffuse reflections reaching the absorber.

For non-normal incidence conditions, ray-tracing results show that the incidence angle modifier (IAM) in the transverse direction (θ_T) increases within the range of 10° to approximately 70°, reaching values of about 1.2–1.3 at 50°, with some dependence on the reflector material. These values are consistent with those obtained experimentally at the BECS facility (for the CPSS configuration), as discussed in a later section.

Table 3
Total, specular and diffuse reflectance of the materials analyzed and optical performance at normal incidence.

Reflectance	High-reflectance aluminum-based (HRAB)	Commercial polished aluminum (CPA)	Aged commercial polished aluminum (ACPA)	Commercial polished stainless steel (CPSS)
Specular	83 %	70 %	40 %	47.5 %
Diffuse	7 %	15 %	35 %	15.5 %
Total	90 %	85 %	75 %	63 %
Optical efficiency results (Tonatiuh) at normal incidence	60.7 %	–	54.2 %	49.8 %
Surplus efficiency due to reflector	34.2 %	–	27.7 %	23.3%

The optical efficiency of the vacuum tubes without a reflector was also evaluated, yielding a value of 26.5%. The additional contribution of the reflector ("surplus efficiency") is defined as the difference between the total optical efficiency and this baseline value.

Overall, the results indicate that aluminum-based reflectors achieve higher optical efficiencies, even with some degree of aging. However, stainless steel remains an attractive option due to its superior durability, lower cost, and higher local availability. A preliminary cost survey indicates that CPSS is approximately half the cost of CPA and more than four times less expensive than HRAB. Nevertheless, a detailed cost–benefit analysis is required to determine the optimal material choice, together with further experimental assessment of long-term aging effects.

The peak efficiency ($\eta_{0,b}$) of the CPC with a stainless steel reflector at ambient conditions is therefore expected to be lower than the initially targeted value of 55%. This is because $\eta_{0,b}$ (approximately 50%, according to ray-tracing simulations) depends not only on optical efficiency but also on thermal losses, since the absorber temperature remains above ambient even when the fluid temperature equals the ambient temperature.

Additional discrepancies between the expected and measured optical efficiencies are due to the reflector geometry. Analysis of a reference CPC collector [30] shows that, despite having a concentration ratio below unity, its geometry resembles a single parabola rather than a true involute. This configuration is expected to yield higher efficiency at normal incidence but lower at off-normal angles (with IAM values close to or below unity). Consistent trends are observed in ray-tracing analyses of parabola–involute geometries with varying acceptance angles, where lower acceptance angles increase normal-incidence efficiency at the expense of off-normal performance.

Overall, these results indicate that assessing the annual energy yield, accounting for CPC geometry, reflector material, and local solar conditions, is required to determine the optimal design.

Calibration of the thermal model and sensitivity analysis of thermal performance. To calibrate the thermal model described in Section 2.2, a modified commercial CPC collector—obtained by replacing the original aluminum reflectors with stainless steel ones of identical geometry [30]—was experimentally tested at the BECS facility [28]. The main fitting parameters were the global heat transfer coefficient at the contact interface between the evaporator wall and the internal aluminum fin, and the absorber emissivity. The calibrated values were 700 $W/m^2.K$ for the heat transfer coefficient and 0.075 for the emissivity. A detailed description of the calibration procedure is provided in another work [26]. These parameters are subsequently used to predict the thermal behavior of the proposed collector design with a concentration ratio close to unity.

Using the calibrated model, a sensitivity analysis was conducted on key design parameters of the first CPC prototype (CR = 1, involute reflector), including flow rate, condenser–socket thermal contact, and fin configuration (i.e., number and thickness of internal aluminum fins within the heat pipe). The results indicate that degradation in fin quality (from the reference to the lowest-performance configuration) and thermal contact (from a reference paste conductivity of 1 to 0.075 W/m·K, with a 0.05 mm clearance) have comparable and significant effects, increasing global thermal resistance and reducing efficiency by about 4% (≈10% lower thermal output) in each case. In contrast, flow rate variations have a minor impact in the proposed design. In extreme conditions, such as a 0.25 mm air gap at the interface, performance degradation becomes much more severe, with a marked increase in absorber temperature that may lead the heat pipe to approach its dry-out limit.

As thermal contact depends on proper paste application and its long-term stability, this aspect requires particular attention. In cases of significant degradation, alternative solutions such as mechanical clamping or U-tube configurations may need to be considered.

Based on the calibrated model, Fig. 6 shows the expected collector efficiency under different scenarios. At normal incidence and 20°C ambient temperature, the field efficiency is ∼35% at 145°C, slightly below the initial 38% estimate, although improved performance at off-normal incidence is expected relative to the reference CPC. The left panel illustrates system sensitivity: the gray curve simulates a reduction in optical efficiency under nominal thermal behavior, while the orange curve depicts a decline in thermal performance under nominal optical efficiency.

The right panel compares different reflector materials, showing that reflectors with higher reflectivity enhance overall performance, although their adoption requires further techno-economic assessment, which is left to future work. Here, dashed lines represent the optical efficiency, which increases with material quality, and their divergence from the solid curves quantifies thermal losses. Notably, thermal losses occur even when the fluid matches the ambient temperature (20°C) because the absorber operates at a higher temperature, dissipating heat to the environment.

First-scale prototype testing and comparison with model results. The results presented in this section correspond to the experimental evaluation of the first assembled CPC prototype (Section 2.2, Fig. 4) at the BECS facility. Tests were conducted for operating temperatures up to 100°C at a flow rate of 5.5 L/min. The resulting performance parameters and associated uncertainties, determined according to Eq. (1) and referenced to the aperture area, are summarized in Table 4 and presented in Fig. 7. The incidence angle modifier (IAM) values reported in Table 4 correspond to the longitudinal (KbL) and transverse (KbT) directions.

Fig. 7 compares the simulated efficiency curve for the CPSS reflector (blue) with the experimental results (black), using Eq. (2) under standard simplifying assumptions (clear-sky conditions, normal incidence, steady state). The solid line corresponds to measured data, while the dashed line represents extrapolation up to 160°C[4]. A discrepancy of approximately 15 percentage points is observed at $T_f = 20°C$.

Despite this gap, the experimental curve exhibits a low slope and negligible curvature, indicating that the global heat loss coefficient remains within the expected range. The analysis therefore focuses on identifying the dominant loss mechanisms through combined optical and thermal modeling.

Potential causes include optical losses due to reflector misalignment or deformation, and increased thermal resistance associated with larger clearances at the condenser–socket interface.

Fig. 6 (right) presents additional efficiency curves illustrating the impact of these effects. A reduction in optical efficiency from 49.8% to 42%, representative of the combined effects of multiple optical degradation mechanisms, and a deterioration of thermal contact —modeled as an increase in the clearance gap from 0.05 mm to 0.25 mm together with a reduction in the effective thermal conductivity of the interface material from 1.0 to 0.2 W/m·K— both result in noticeable performance degradation. However, neither effect alone is sufficient to fully explain the observed discrepancy.

The reduced optical efficiency of 42% was estimated through ray-tracing simulations using Tonatiuh, considering the cumulative effect of several possible optical losses. Starting from the baseline optical efficiency of 49.8% under ideal alignment and normal incidence, a 10 mm lateral misalignment reduces the efficiency to 44.9%, while a 10 mm downward displacement lowers it to 45.6%. In addition, dust accumulation was estimated to decrease the efficiency to 47.0%, assuming a reduction in reflector reflectivity from 63% to 60% and glass transmissivity from 89% to 86%, corresponding to values reported in the literature [50].

The thermal resistance of the vacuum and manifold insulation appears to remain within the expected range, suggesting that the dominant losses are associated with the optical path rather than with heat dissipation to the environment. Additional factors may include contamination of reflective surfaces or absorber tubes during assembly or transport, as well as possible differences between the heat pipes used in the reference collector (for model calibration) and those in the prototype. Although supplied by the same vendor, variations in optical or thermal properties cannot be excluded.

The transverse incidence angle modifier, $K_{bT}(\theta)$, also exhibited an increasing trend, consistent with ray-tracing predictions, highlighting the importance of accounting for off-normal incidence in performance evaluation.

Given the significant gap between the expected (∼48%) and measured (33.5%) $\eta_{0,hem}$, a second prototype is under construction to further investigate these discrepancies. Future work will focus on targeted diagnostics and design improvements addressing the identified optical and thermal issues. The combined use of numerical modeling and experimental validation remains essential for optimizing the collector design and progressing toward industrial application at the target steam pressure.

Collector design analysis and improvement pathways

Overall, the combined optical characterization, numerical modeling, and experimental testing provide a consistent understanding of the collector performance and its main limitations. While aluminum-based reflectors offer higher optical efficiency, stainless steel remains a competitive alternative due to its durability, cost, and local availability. The calibrated thermal model proves to be an effective tool for performance prediction and for identifying critical design parameters, particularly the thermal contact at the heat pipe–manifold interface.

Experimental results from the first prototype confirm the general trends predicted by the model, including heat loss behavior and incidence angle effects. However, the significant discrepancy in peak efficiency highlights the strong sensitivity of the system to optical and assembly-related factors.

These findings motivate a refinement of the manufacturing and assembly processes. The geometric accuracy of the CPC profile will be reviewed in future prototypes, supported by the development of a dedicated in-situ reflector evaluation device. In parallel, improvements in reflector fabrication and mounting procedures will be implemented. On the thermal side, manufacturing tolerances in the manifold sockets will be refined to minimize contact resistance. Experience gained during the construction of the first prototype—particularly regarding welding techniques to avoid deformation of the copper sockets—will be incorporated into subsequent designs to ensure consistent clearances and improved thermal coupling between the heat pipe condensers and the manifold. The condenser–socket interface is identified as a critical point not only for performance but also for reliability and maintenance, potentially motivating alternative design solutions such as mechanical clamping or U-tube configurations.

Additional experimental work is underway to evaluate the performance of evacuated tubes from different manufacturers without reflectors, enabling direct comparison of absorptance and thermal efficiency independently of reflector contributions. Finally, a detailed

[4] As mentioned in section 2.2 (Experimental test methods), acceptable uncertainty is expected in the extrapolation until ∼130°C, while higher uncertainty is expected beyond that fluid temperature.

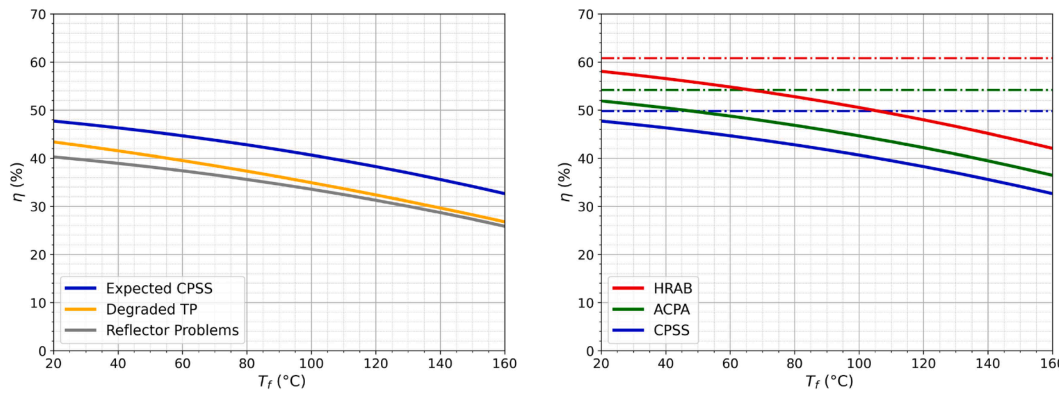

Fig. 6. Efficiency curves for the proposed CPC collector. Left: the expected efficiency (per aperture area) is compared with possible problems that could lower it. Right: expected efficiency for different reflector materials.

Table 4
Value and uncertainty of the parameters obtained from the first CPC prototype test in BECS (referred to aperture area).

Parameter	$\eta_{0,b}$	K_d	$\eta_{0,hem}$	a_1 (W/m^{2}K)	a_2 (W/m^{2}K^2)		
Value	0.335	0.997	0.335	0.434	0		
Uncertainty	0.003	N.C	0.003	0.062	N.C		
θ_L / θ_T	0	10	20	30	40	50	60
K_{bL}	1.00	1.00	1.00	1.00	1.00	1.00	-
K_{bT}	1.00	1.00	1.04	1.09	1.15	1.22	1.28

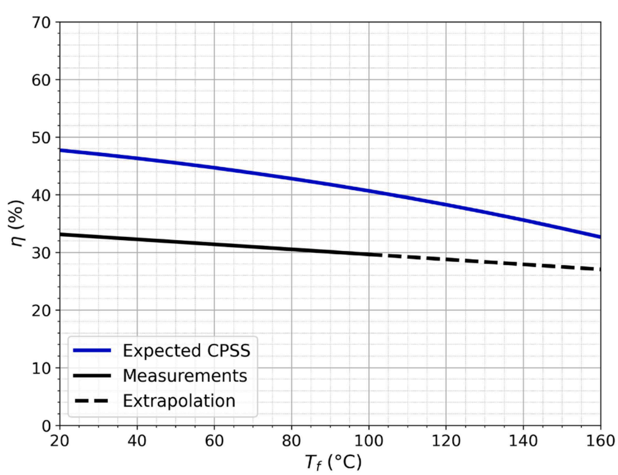

Fig. 7. The simulated efficiency curve (in blue) is compared to the measurements and their extrapolation (in black).

cost–benefit analysis of alternative reflector materials, particularly aluminum-based solutions, and reflector shapes, is planned. This will include annual energy yield assessments under representative meteorological conditions to identify the optimal trade-off between performance and cost.

Concrete mix properties and TES performance

Results from the thermal conductivity measurements and numerical TES simulations described in Section 2.3 are presented here. Further details can be found in [27].

Concrete thermal conductivity

A total of 89 thermal conductivity measurements at ambient temperature were performed across all concrete samples, yielding an average value of 2.23 W/m·K for the entire sample set. The highest conductivity was observed in samples without metallic fibers, with $k_0 = 2.65 \pm 0.09$ W/m·K (19 measurements, standard deviation of 0.18 W/m·K). The lowest values correspond to the 50 and 250 kg/m^3 fiber content groups, with $k_{50} = 1.97 \pm 0.28$ W/m·K (7 measurements, standard deviation of 0.31 W/m·K) and $k_{250} = 2.07 \pm 0.13$ W/m·K (38 measurements, standard deviation of 0.40 W/m·K), respectively. Uncertainties represent 95% confidence intervals assuming a Student's t-distribution. It should be noted that potential systematic errors may affect the reliability of these results.

The measurement procedure proved challenging. Reliable measurements require good thermal contact between the needle probe and the hole wall, typically ensured by properly applying thermal paste. However, due to the geometry of the hole (6 mm diameter and closed-end), complete air removal during probe insertion could not be guaranteed. In addition, the measurements showed strong variability between consecutive tests, particularly when insufficient time was allowed for the probe and specimen to return to thermal equilibrium. As a result, repeatability issues were observed. Consequently, the reported thermal conductivity values should be regarded as preliminary; further testing is required in order to reduce measurement uncertainty.

Contrary to expectations, the addition of metallic fibers not only failed to increase but appears to reduce thermal conductivity. This behavior may be attributed to increased porosity associated with fiber incorporation. However, given the aforementioned measurement limitations and repeatability issues, no definitive conclusions can be drawn from the conductivity data alone. Independent mass and volume measurements indicate a negative correlation between fiber content and density, supporting the porosity hypothesis.

Future work will focus on thermal conductivity measurements using alternative methods, as well as on the determination of heat capacity.

Expected charging behavior and configuration

The preliminary design phase (Section 2.3) resulted in a set of TES configurations with varying pipe length, diameter, and number, all providing a total heat transfer area of 12 m^2. Based on numerical evaluation of thermal performance, as well as fabrication cost and pressure drop considerations, a configuration consisting of two parallel 1/2″ SCH 40 steel pipes with a total length of 179.4 m (89.7 m each) was initially selected. Further analysis, considering available cost and pressure drop margins, led to an increase in pipe length to 107.6 m per pipe (while maintaining the same concrete mass), resulting in a total heat transfer area of 14.4 m^2 embedded in a concrete volume of 2.73 m^3.

The evolution of the dimensionless temperature distribution (determined with Eq. 3) during charging is illustrated in Fig. 8 at different time intervals (10 min, 1 h, 2 h, and 3 h), showing the dimensionless temperature of the pipe domain (steel) and the minimum of the concrete domain. At early stages, significant radial and axial temperature

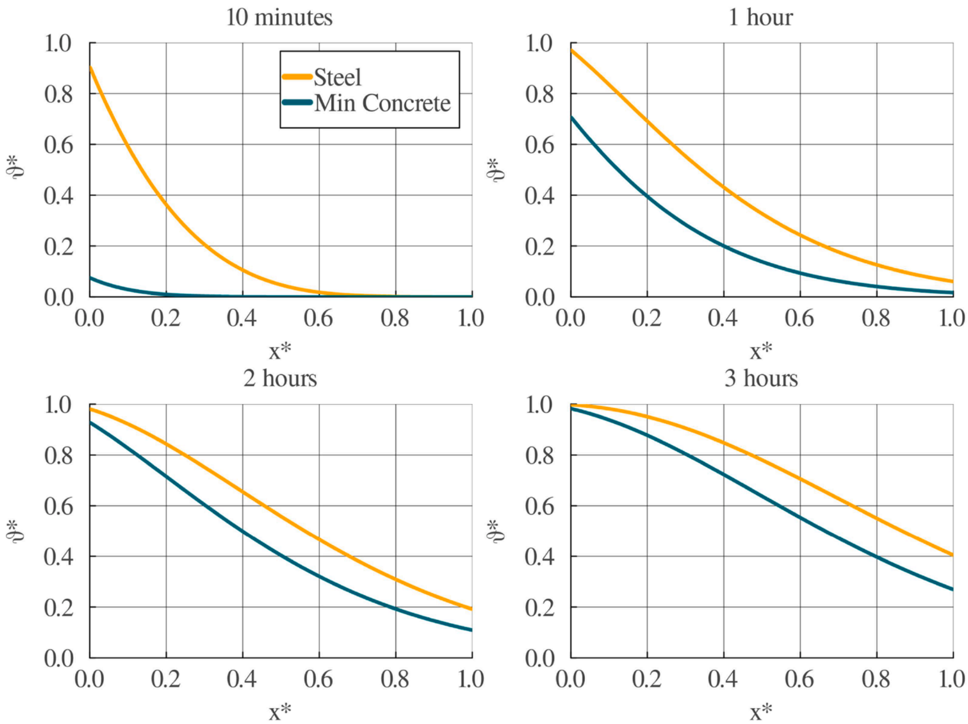

Fig. 8. Storage unit temperature distribution during the charging stage at 10 min, 1 h, 2 h and 3 h, based on simulation results.

gradients are observed. As charging progresses, radial gradients decrease rapidly, while axial stratification persists, supporting the initial assumption of approximately uniform temperature differences over large sections of the exchanger. This behavior confirms the development of thermal stratification, with clearly distinguishable “hot” and “cold” regions within the device.

The simulated temperature distributions are also used to evaluate the preliminary (analytic) design approach, which assumes a constant integrated temperature difference, ΔT_{mean}. This parameter is calculated (with Eq. 6) at 10-minute intervals over the 3-hour charging period, yielding an average value of 3.71°C, ranging from 2.65 °C at the end of the charging period to 4.40 °C near the beginning. Although ΔT_{mean} is not strictly constant, the largest deviations occur at the beginning and end of the charging process, with a sudden rise from 0 to 4.40 °C followed by a slow decay to 2.65 °C, supporting the validity of the simplifying assumption of a nearly constant ΔT_{mean} during most of the charging period for the initial analytical dimensioning.

Fig. 9 (a) presents the heat charging rate (HR), defined as the time derivative of E (Eq. 5), and the SOC, calculated using Eq. (4), as functions of time. As expected, HR decreases over time due to the reduction in the average temperature difference, dropping from the design value of 10 kW to approximately 6 kW after 3 hours of operation (with a mean value of 8.37 kW), reaching a final SOC of 66.6%. This decay highlights the need for appropriate operational strategies to maintain performance during the final stages of charging, as it is directly related to outlet temperature; high outlet temperature may lead to fluid evaporation inside the solar collector manifolds. Operational strategies could include flow rate regulation or alternative heat management approaches.

Since the experimental determination of thermal conductivity was affected by methodological limitations and remains preliminary, a sensitivity analysis was performed to assess the impact of this parameter on TES performance. The same storage configuration was simulated using thermal conductivity values ranging from 1.5 to 2.5 W/m·K, and the resulting effects on state of charge (SOC) evolution and mean heat rate (HR) are also shown in Fig. 9 (b).

Increasing the thermal conductivity from the baseline value of 2.0 W/m·K to 2.5 W/m·K increases the mean heat rate and final SOC by approximately 2.7% (from 8.37 to 8.59 kW and from 66.6% to 68.3%, respectively). Conversely, reducing the conductivity to 1.5 W/m·K decreases these values by approximately 4% (8.03 kW and 64.0%, respectively). These relatively small variations indicate that, within the range considered, TES performance is only moderately sensitive to

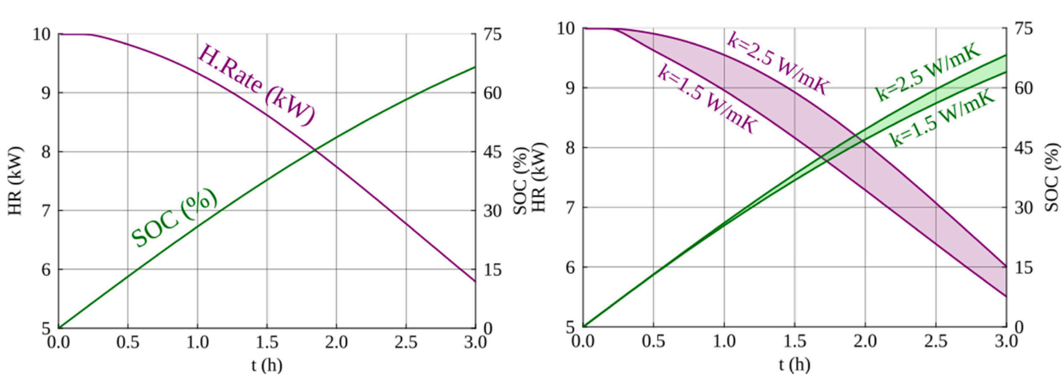

Fig. 9. (a) Thermal battery SOC and heat transfer rate over time during the charging stage (with k = 2.0 W/m K), (b) thermal conductivity sensitivity.

thermal conductivity. Therefore, the uncertainty associated with the current conductivity measurements is not expected to significantly affect the main conclusions regarding charging and discharging behavior.

It should be emphasized that these results correspond to a single charging process starting from a uniform "cold" initial condition (fully discharged). Further analysis should consider variable fluid flow rates and inlet temperatures, as well as multiple charge–discharge cycles under different weather conditions and heat demand profiles. In addition, future experimental campaigns will enable validation of the numerical model and assessment of the prototype performance. Overall, these results should be regarded as preliminary, as model validation and a more robust determination of the thermal properties remain as future work.

To implement the proposed design within a compact footprint, a zigzag tube arrangement is adopted, as schematized in Fig. 10. The TES unit is divided into five equal slabs separated by 50 mm thermal insulation layers to preserve axial stratification by limiting thermal interaction between consecutive tube passes. The entire unit is enclosed within 300 mm of external insulation, designed to maintain the storage temperature above 135°C for approximately one week starting from a fully charged state under winter conditions.

Overall, the numerical and experimental results provide a consistent basis for the selected TES design, although further validation under cyclic operation is still required.

The analysis of thermal stresses in the TES concrete matrix and tubes remains future work. Once the prototype has been constructed, the effects of TES thermal cycling will be evaluated. Based on operational data and potential material testing, system control strategies may be adjusted, and design modifications may be proposed to facilitate maintenance and mitigate the adverse effects associated with thermal cycling.

Conclusions and outlook

This work presented the design and preliminary assessment of a Solar Heat for Industrial Processes (SHIP) pilot system in Uruguay, designed to operate at temperatures above 100°C. The proposed system integrates Compound Parabolic Collector (CPC) technology with a concrete-based thermal energy storage (TES) unit within a closed-loop pressurized fluid circuit designed to emulate industrial steam demand. Both the CPC field and the TES unit were developed through a joint industry-academia engineering effort. The resulting system configuration, component sizing, and operating strategies constitute a consistent framework for coupling solar heat generation and storage while prioritizing local manufacturability, operational simplicity, and compliance with safety constraints.

The design methodology, combining simplified analytical approaches, numerical simulations, and experimental characterization, proved useful for component sizing and for identifying critical design parameters at an early stage. A key contribution of the work is the integration of these methodologies within a unified design framework aimed at representative industrial heat supply conditions. This approach facilitates the identification of dominant physical mechanisms and supports the transition from component-level studies toward pilot-scale system development.

Experimental characterization of the 3.9 m^2 CPC prototype yielded a peak optical efficiency of 33.5% ($\eta_{o,hem}$), below the expected 48–50%. However, the low slope of the efficiency curve indicates that thermal losses remain within the expected range, suggesting that optical and manufacturing factors—particularly reflector geometry and manifold assembly tolerances—constitute the main performance limitations. The identification of these sensitivities helps define quality requirements for future local manufacturing and highlights the value of local experimental infrastructure for collector development and validation. Although the characterization of the first collector prototype identified the main performance limitations and provides guidance for the next design iteration, its measured efficiency does not yet allow conclusions regarding the technical or economic viability of a full-scale installation. Such an assessment will require improved collector prototypes, experimental validation of the complete integrated system, and a dedicated techno-economic analysis.

For thermal storage, preliminary measurements yielded thermal conductivity values up to 2.65 W/m·K for selected concrete formulations. The observed reduction with increasing fiber content is likely associated with increased porosity, although additional testing is required to confirm this trend and to assess performance at elevated temperatures. Preliminary numerical results indicate that the selected TES geometry is capable of supporting thermal stratification and effective charge/discharge operation. Nevertheless, these findings remain preliminary, as construction, experimental testing, and model validation of the complete TES unit are still pending.

The present results support the conceptual design and preliminary assessment of the proposed SHIP system. Nevertheless, experimental validation of the fully integrated pilot plant remains necessary before conclusions can be drawn regarding its overall technical performance. The project is currently transitioning toward integrated pilot-scale operation. A second collector prototype is under construction to address identified optical and thermal contact limitations, and the full 24 m^2, ~10 kW collector field and TES unit is expected to become operational shortly, enabling system-level evaluation.

Future work will therefore include experimental validation of the integrated system, refinement of numerical models, and assessment of alternative design solutions to improve performance, reliability, and maintainability.

In addition, although cost considerations have influenced several design decisions throughout the project—including technology selection, material choices, and manufacturability criteria—a dedicated techno-economic assessment has not yet been performed. Consequently, the economic viability of the proposed solution, including its proximity to target collector costs and its competitiveness under representative operating conditions, cannot yet be established. A comprehensive techno-economic analysis and scalability assessment based on experimental data from the pilot plant will therefore constitute another major focus of future work once integrated system operation has been completed.

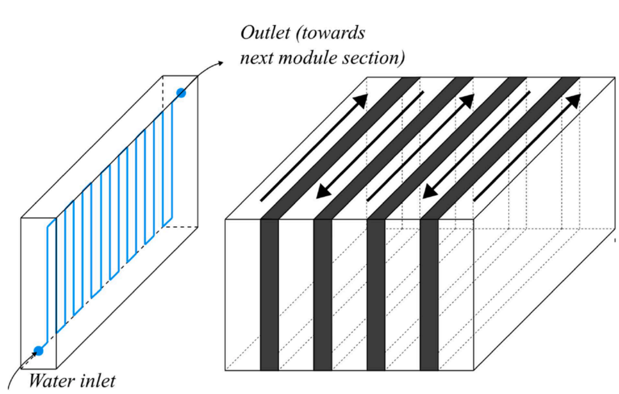

Fig. 10. Thermal battery exchanger design, composed of 5 sections separated by thermal insulating material.

Declaration of generative AI and AI-assisted technologies in the writing process

During the preparation of this work, the author(s) used ChatGPT and Gemini in order to improve the readability and language of the manuscript. After using this tool/service, the author(s) reviewed and edited the content as needed and take(s) full responsibility for the content of the published article.

CRediT authorship contribution statement

Pedro Galione: Writing – review & editing, Writing – original draft, Supervision, Project administration, Methodology, Investigation, Funding acquisition, Conceptualization. **Germán Navarrete:** Writing – review & editing, Writing – original draft, Visualization, Methodology, Investigation. **Renzo Guido Cruz:** Writing – review & editing, Writing – original draft, Visualization, Validation, Software, Methodology, Investigation. **Federico Licandro:** Writing – review & editing, Writing – original draft, Visualization, Methodology, Investigation. **Juan Rodríguez Muñoz:** Writing – review & editing, Writing – original draft, Resources, Methodology, Investigation. **Italo Bove:** Writing – review & editing, Supervision, Investigation. **Joaquin Buydid:** Writing – original draft, Methodology, Investigation. **Sebastián Lillo:** Writing – original draft, Investigation, Conceptualization. **Pablo Dellicompagni:** Writing – review & editing, Writing – original draft, Supervision. **Marcos Hongn:** Writing – review & editing, Supervision. **Loreto Valenzuela:** Writing – review & editing, Supervision, Methodology. **Emmanuel Romano:** Supervision, Resources, Project administration, Methodology, Investigation, Funding acquisition, Conceptualization.

Declaration of competing interest

Given her role as member of the Editorial Board, Loreto Valenzuela had no involvement in the peer review of this article and had no access to information regarding its peer review. Full responsibility for the editorial process for this article was delegated to another journal editor. If there are other authors, they declare that they have no known competing financial interests or personal relationships that could have appeared to influence the work reported in this paper.

The rest of the authors do not have any conflict of interest to declare.

Acknowledgements

The authors gratefully acknowledge the National Agency of Research and Innovation (ANII) of Uruguay for its financial support through the project ANII_ART_X_2023_1_179571 “Calor solar y acumulación para la industria”. The authors acknowledge financial support from the CSIC Group’s Program, Universidad de la República, Uruguay.

References

[1] D. De León, P. Galione, Thermo-economic evaluation of solar concentrating technologies for industrial process heat production in Uruguay, in: In Proceedings of the ISES Solar World Congress 2019 / IEA SHC International Conference on Solar Heating and Cooling for Buildings and Industry, International Solar Energy Society (ISES), Santiago, Chile, 2019. https://doi.org/10.18086/swc.2019.12.03.

[2] Concentra. Solar, Mercado potencial en España y aplicaciones en tecnologías solares de concentración de media temperatura. Plataforma Tecnológica de la Energía Solar Térmica de Concentración, 2015. https://www.solarconcentra.org/mercado-potencial-en-espana-y-aplicaciones-en-tecnologias-solares-deconcentracion-de-media-temperatura/.

[3] W. Weiss, M. Spörk-Dür. Solar Heat Worldwide 2024: Global Market Development and Trends 2023 – Detailed Market Figures 2022, AEE – Institute for Sustainable Technologies, IEA Solar Heating & Cooling Programme, 2024. https://doi.org/10.18777/ieashc-shww-2024-0001.

[4] Solar heat for industrial processes (SHIP): Technology position paper. Task 64 – Solar Process Heat, IEA Solar Heating and Cooling Technology Collaboration Programme, 2024. https://task64.iea-shc.org/Data/Sites/1/publications/IEA-SHC-Task64-Technology-Position-Paper-SHIP-2024-01.pdf.

[5] C. McMillan, C. Schoeneberger, J. Zhang, P. Kurup, E. Masanet, R. Margolis, S. Meyers, M. Bannister, E. Rosenlieb, W. Xi. Opportunities for solar industrial process heat in the United States (NREL/TP-6A20-77760), National Renewable Energy Laboratory, Golden, CO, 2021. https://doi.org/10.2172/1762440.

[6] PROTERMOSOLAR. IDAE, Guía de energía solar térmica de concentración para procesos industriales (Guías IDAE 034), Instituto para la Diversificación y Ahorro de la Energía (2025), in: https://www.idae.es/publicaciones/guia-de-energia-solar-termica-de-concentracion-para-procesos-industriales.

[7] J.A. Duffie, W.A. Beckman. Solar engineering of thermal processes, 4th ed., John Wiley & Sons, Inc, 2013 https://doi.org/10.1002/9781118671603.

[8] S.A. Kalogirou, Solar energy collectors, in: Solar energy engineering: Processes and systems, 2nd ed., Academic Press, 2014, pp. 125–220.

[9] E. Cardozo Montes de Oca, G. López Chiossoni, G. Morales Gil, Diseño y evaluación termo-económica de un concentrador cilindro-parabólico para aplicaciones industriales de media temperatura [Tesis de grado], Montevideo: Universidad de la República, Facultad de Ingeniería IIMPI (2025). https://hdl.handle.net/20.500.12008/51985.

[10] I. Bove Vanzulli, Eficiencia de sistemas de conversión solar-térmica (Proyecto FSE_1_2013_1_10649, Fondo Sectorial Energía). Facultad de Ingeniería, Universidad de la República (2013). https://www.fing.edu.uy/~italo/Proyecto_EST_FSE-20130718_FINAL.pdf.

[11] Roca Acosta y Lara, J.M. (2025). Energía solar concentrada para calor de procesos [Tesis de maestría]. Montevideo: Universidad de la República, Facultad de Ingeniería. https://hdl.handle.net/20.500.12008/48648.

[12] P. Horta, C. Brunner, K. Kramer, E. Frank, IEA/SHC T49 activities on process heat collectors: Available technologies, technical-economic comparison tools, operation and standardization recommendations, Energy Procedia 91 (2016) 630–637, https://doi.org/10.1016/j.egypro.2016.06.217.

[13] PUC, Chile (Pontificia Universidad Católica de Chile). (2020). Choosing by advantages [online course]. Coursera. https://www.coursera.org/learn/camino-excelencia-gestion-proyectos.

[14] G.H. Bargale, N.K. Chougule, Experimental investigation of the performance of compound parabolic collector (CPC) for low and medium temperature application, Energy Rep. 9 (Suppl. 11) (2023) 97–103, https://doi.org/10.1016/j.egyr.2023.08.053.

[15] M. Farhan, M.I. Shahid, F. Jamil, M. Usman, M.A. Mujtaba, M.W. Saleem, S. Nasir Shah, S. Saghir, A.A. Yusuf, M. Mousa, A.S. El-Shafay, Performance evaluation of compound parabolic solar collector using different nanofluids: An experimental study, Front. Energy Res. 10 (2022) 951233, https://doi.org/10.3389/fenrg.2022.951233.

[16] H. Riaz, M. Ali, J. Akhter, N.A. Sheikh, M. Rashid, M. Usman, Numerical and experimental investigations of an involute shaped solar compound parabolic collector with variable concentration ratio, Renew. Energy 216 (2023) 119025, https://doi.org/10.1016/j.renene.2023.119025.

[17] M. Shehryar, M. Ali, F. Ali, S. Ahmad, D. Ahmad, S. Ahmed, O. Iftikhar, Design and experimental investigation of thermosiphoning heat transfer through nanofluids in compound parabolic collectors, J. Eng. Res. 10 (2022), https://doi.org/10.36909/jer.ICEPE.19537 (ICEPE Special Issue).

[18] J. Moreno-SanSegundo, M. Martín-Sómer, J. Marugán, Dynamic concentration factor: A novel parameter for the rigorous evaluation of solar compound parabolic collectors, Chem. Eng. J. 437 (Part 2) (2022) 135360, https://doi.org/10.1016/j.cej.2022.135360.

[19] B. Widyolar, L. Jiang, Y. Bhusal, J. Brinkley, R. Winston, Solar thermal process heating with the external compound parabolic concentrator (XCPC) – 45 m^2 experimental array performance, annual generation (kWh/m^2-year), and economics, Sol. Energy 230 (2021) 131–150, https://doi.org/10.1016/j.solener.2021.10.027.

[20] D. Laing, D. Lehmann, C. Bahl, Concrete storage for solar thermal power plants and industrial process heat. https://elib.dlr.de/57976/.

[21] M. Gea, F. Tilca, C. Placco, R. Caso, A. Machaca, L. Saravia, Acumulación térmica en hormigón de la energía solar captada por un concentrador tipo Fresnel lineal para generación de vapor. Avances en Energías Renovables y Medio Ambiente 13, 2009, pp. 113–119. http://sedici.unlp.edu.ar/handle/10915/96888.

[22] P. Dellicompagni, M. Hongn, L. Saravia, M. Altamirano, C. Placco, M. Gea, D. Hoyos, H. Bárcena, H. Suligoy, C. Fernández, R. Caso, Concentrador solar térmico Fresnel lineal de San Carlos, Salta. Primeros ensayos de operación y funcionamiento (172 m^2), Avances en Energías Renovables y Medio Ambiente 20 (2016) 1–12. http://sedici.unlp.edu.ar/handle/10915/66744.

[23] S. Freund, M. Abarr, J.D. McTigue, K.L. Frick, A. Mathur, D. Reindl, A. Van Asselt, G. Casubolo, Thermal energy storage, in: K. Brun, T.C. Allison, R. Dennis (Eds.), Thermal, mechanical, and hybrid chemical energy storage systems, Academic Press, 2021, pp. 65–137, https://doi.org/10.1016/B978-0-12-819892-6.00003-4.

[24] L.F. Cabeza, D. Vérez, G. Zsembinszki, E. Borri, C. Prieto, Key challenges for high temperature thermal energy storage in concrete—First steps towards a novel storage design, Energies 15 (13) (2022) 4544, https://doi.org/10.3390/en15134544.

[25] S. Wang, A. Abdulridha, J. Bravo, C. Naito, S. Quiel, M. Suleiman, C. Romero, S. Neti, A. Oztekin, Thermal energy storage in concrete: Review, testing, and simulation of thermal properties at relevant ranges of elevated temperature, Cement Concr. Res. 166 (2023) 107096, https://doi.org/10.1016/j.cemconres.2023.107096.

[26] R.G. Cruz, J.M. Rodríguez-Muñoz, P.A. Galione. Analysis of heat pipes for CPC solar collectors to provide heat for industrial processes, International Solar Energy Society (ISES, Fortaleza, Brazil, 2025, https://doi.org/10.18086/swc.2025.02.03.

[27] F.H. Licandro, P.A. Galione, J.A. Buydid, E. Romano. Design of a concrete-based sensible heat storage module prototype for solar heat. In Proceedings of the ISES Solar World Congress 2025, International Solar Energy Society (ISES), Fortaleza, Brazil, 2025. https://doi.org/10.18086/swc.2025.02.11.

[28] J.M. Rodríguez-Muñoz, I. Bove, P.A. Galione. General incident angle modifier model for quasi-dynamic testing of solar thermal collectors, International Solar Energy Society (ISES, Fortaleza, Brazil, 2025. https://doi.org/10.18086/swc.2025.02.15.

[29] ISO. (2025). Solar energy — Solar thermal collectors — Test methods (ISO 9806: 2025). International Organization for Standardization. https://www.iso.org/standard/78801.html.

[30] Intertek. Test report No. 180710029GZU-001: Zhejiang Shentai Solar, Energy Co., Ltd., collector models SHC8X–SHC24X. Intertek Testing Services Shenzhen Ltd., Guangzhou Branch, China, 2021.

[31] Solartechnik. Ritter. Product catalogue: Evacuated tube collectors: CPC OEM, CPC INOX, CPC XL INOX. 2025/2026, Ritter Solartechnik GmbH & Co. KG. https://www.ritter-solartechnik.de/en/evacuatedtube- collectors/, 2025.

[32] T.L. Bergman, A.S. Lavine, F.P. Incropera, D.P. DeWitt. Fundamentals of heat and mass transfer, 8th ed., Wiley, 2018.

[33] Power Piping (ASME B31.1-2020), The American Society of Mechanical Engineers, 2020. https://www.asme.org/codes-standards/find-codes-standards/b31-1-power-piping.

[34] DNE (Ministerio de Industria, Uruguay) Energía y Minería, Especificaciones técnicas uruguayas de instalaciones solares térmicas (ETUS). Aprobadas por Resolución MIEM N.º 72/014, de 14 de mayo de 2014. Ministerio de Industria, Energía y Minería (2014).

[35] I.E. Idel'chik. Handbook of hydraulic resistance, 3rd ed., Begell House, Inc, 1996.

[36] Peuser, F.A., Remmers, K.-H., & Schunss, M. (2005). Sistemas solares térmicos: Diseño e instalación. Progensa.

[37] A. Faghri. Heat pipe science and technology, Global Digital Press, 1995.

[38] Y. Tripanagnostopoulos, M. Souliotis, Integrated collector storage solar systems with asymmetric CPC reflectors, Renew. Energy 29 (2) (2004) 223–248, https://doi.org/10.1016/S0960- 1481(03)00195-2.

[39] M.J. Blanco, J.M. Amieva, A. Mancillas, The Tonatiuh software development project: An open source approach to the simulation of solar concentrating systems. In Proceedings of the ASME 2005 International Mechanical Engineering Congress and Exposition (IMECE2005), in: Computers and Information in Engineering, ASME, 2005, pp. 157–164, https://doi.org/10.1115/IMECE2005-81859.

[40] I. Ramón-Álvarez, S. Sánchez-Delgado, I. Peralta, A. Caggiano, M. Torres-Carrasco, Experimental and computational optimization of eco-friendly mortar blocks for high temperature thermal energy storage of concentrated solar power plants, J. Energy Stor. 71 (2023) 108076, https://doi.org/10.1016/j.est.2023.108076.

[41] H.G. Weller, G. Tabor, H. Jasak, C. Fureby, A tensorial approach to computational continuum mechanics using object-oriented techniques, Comp. Phys. 12 (6) (1998) 620–631, https://doi.org/10.1063/1.168744.

[42] Carpemar, Propylene Glycol Coolant NSF [Ficha técnica]. https://carpemar.com/es/productos/9-productos/26-propileneglycol-coolant-nsf.html.

[43] I. Asadi, P. Shafigh, Z.F.B. Abu Hassan, N.B. Mahyuddin, Thermal conductivity of concrete - A review, J. Build. Eng. 20 (2018) 81–93, https://doi.org/10.1016/j.jobe.2018.07.002.

[44] D.J. Cook, C. Uher, The thermal conductivity of fibre-reinforced concrete, Cem. Concr. Res. 4 (4) (1974) 497–509, https://doi.org/10.1016/0008-8846(74)90001-5.

[45] V.K.R. Kodur, M.A. Sultan, Effect of temperature on thermal properties of high-strength concrete, J. Mater. Civil Eng. 15 (2) (2003) 101–107, https://doi.org/10.1061/(ASCE)0899-1561(2003)15:2(101).

[46] S. Liang, G. Song, H. Du, X. Li, J. Liu, Y. Wei, Mesoscale FE analysis of thermal conductivity of steel fiber-reinforced cementitious materials considering fiber–matrix interface and pore effects, Cem. Concr. Compos. 142 (2023) 105194, https://doi.org/10.1016/j.cemconcomp.2023.105194.

[47] Y. Zhang, Q. Lei, W. Zhao, Y. Yang, Y. Wang, Z. Yan, H. Zhu, J.W. Ju, An improved micromechanical model for the thermal conductivity of multi-scale fiber reinforced ultra-high performance concrete under high temperatures, Mater. Des. 236 (2023) 112503, https://doi.org/10.1016/j.matdes.2023.112503.

[48] Standard test method for determination of thermal conductivity of soil and soft rock by thermal needle probe procedure (ASTM D5334-14), ASTM International (2014). https://www.astm.org/d5334-14.html.

[49] TEMPOS manual, METER Group, Inc, 2020. https://www.thermoconceptsarl.com/wp-content/uploads/2020/12/TEMPOS_Manual_Web.pdf.

[50] A.A. Hegazy, Effect of dust accumulation on solar transmittance through glass covers of plate-type collectors, Renew. Energy 22 (4) (2001) 525–540, https://doi.org/10.1016/S0960-1481(00)00093-8.